Geochemical Perspectives Letters

© 2021 The Authors
Published by the European Association of Geochemistry

# Selenium isotope evidence for pulsed flow of oxidative slab fluids

S. König[1*], C. Rosca[1], T. Kurzawa[1], M.I. Varas-Reus[1], B. Dragovic[2], R. Schoenberg[1,3], T. John[4*]

OPEN ACCESS
doi: 10.7185/geochemlet.2110

## Abstract

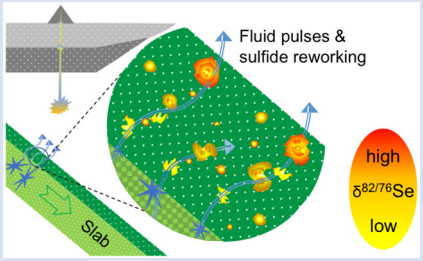


Isotope systematics of the redox sensitive and chalcophile element selenium (Se) were investigated on exhumed parts of subducted oceanic lithosphere to provide new constraints on slab dehydration conditions during subduction. The samples show increasing $\delta^{82/76}Se_{NIST3149}$ with higher abundances of fluid mobile elements, comprising a larger range (−1.89 to +0.48 ‰) than that of mantle (−0.13 ± 0.12 ‰) and altered ocean crust (−0.35 to −0.07 ‰). Our data point to pronounced, local scale redox variations within the subducting crust, wherein oxidative fluids dissolve sulfides and mobilise oxidised Se species. Subsequently recrystallising sulfides preferentially incorporate isotopically lighter, reduced Se, which shifts evolving fluids and late stage sulfides to higher $\delta^{82/76}Se_{NIST3149}$. Redistribution of Se by repeated cycles of sulfide reworking within the subducted crust can be reconciled with episodes of oxidised fluid pulses from underlying slab mantle in modern subduction zones.

Received 20 October 2020 | Accepted 13 February 2021 | Published 9 March 2021

## Introduction

The development of a habitable Earth with its atmosphere-ocean system is closely linked to plate tectonics and the efficient exchange of elements between interior and exterior reservoirs. Key aspects are the subduction cycles of water, carbon and sulfur and the redox state of arc magmas. It is particularly debated if the oxidised nature of arc magmas is due to oxidised slab components or related to secondary processes during the evolution of arc melts (*e.g.*, Lee *et al.*, 2012; Chen *et al.*, 2019; Tollan and Hermann, 2019). Likewise, different models for sulfate- and $^{34}S$-enriched arc lavas involve either slab-derived sulfur flux into the overlying mantle wedge or crustal assimilation by ascending magma (*e.g.*, Lee *et al.*, 2012; Pons *et al.*, 2016). Recent *in situ* S isotope investigations of sulfides from exhumed high pressure rocks reveal prograde subduction related mobilisation and re-entrapment of S during (partial) sulfide breakdown and recrystallisation, resulting in differences in $\delta^{34}S$ of almost 40 ‰ (Evans *et al.*, 2014; Su *et al.*, 2019; Li *et al.*, 2020; Walters *et al.*, 2020), with contrasting data for different localities suggesting either oxidised, $SO_2$- and $CO_2$-rich or reduced, $H_2S$-rich fluid involvement (see also Piccoli *et al.*, 2019).

To further elucidate the redox role of slab-derived components, we combine the novel tool of stable selenium isotopes with a suite of well characterised high pressure rocks of oceanic origin. In comparison to other redox sensitive elements like Mo, S and Fe, Se combines the characteristics of being chalcophile and a trace element that does not act as a major constituent of sulfide. Selenium, therefore, participates in sulfide dissolution-recrystallisation processes within the slab as a witness without being biased as a major constituent of a mineral. Moreover, the transition to selenite (oxidised Se species; $SeO_3^{2-}$; see S-Se species stability fields in Fig. 1) occurs at even higher $fO_2$ compared to the transition to sulfate (oxidised S species; $SO_4^{2-}$). Thus, Se isotope fractionation reflects a strong reduction of at least selenite to selenide from originally higher $fO_2$ than the sulfate-sulfide transition (Fig. 1). Selenium isotopes may thus be useful in constraining the conditions during slab fluid-mediated sulfide redistribution, in particular, if more pronounced redox variations occur in fluids that so far remained beyond the scope of S isotope systematics (König *et al.*, 2019) and previously employed, lithophile (*e.g.*, Mo-Li-N-Tl) stable isotopes in subduction related studies.

The Raspas Complex in SW Ecuador resembles a deeply subducted (~60 km) ophiolite complex that formed during the early Cretaceous at the South American margin. Trace element and radiogenic isotope data revealed that the ophiolite consists of depleted abyssal oceanic mantle, oceanic crust (MORB-type eclogites), associated seamounts (blueschists), and sedimentary cover (John *et al.*, 2010; Halama *et al.*, 2011). The entire complex was metamorphosed at HP/LT conditions (~600 °C and *ca.* 2.0 GPa) and most of the rocks experienced subduction related, prograde dehydration related intra-slab fluid flow during burial (John *et al.*, 2010; Halama *et al.*, 2011; Herms *et al.*, 2012;

1. Isotope Geochemistry Group, Dept. of Earth Sciences, University of Tuebingen, Germany
2. School of the Earth, Ocean and Environment, University of South Carolina, USA
3. Department of Geology, University of Johannesburg, South Africa
4. Institut für Geologische Wissenschaften, Freie Universitaet Berlin, Germany
* Corresponding author (email: stephan.koenig@uni-tuebingen.de; timm.john@fu-berlin.de)

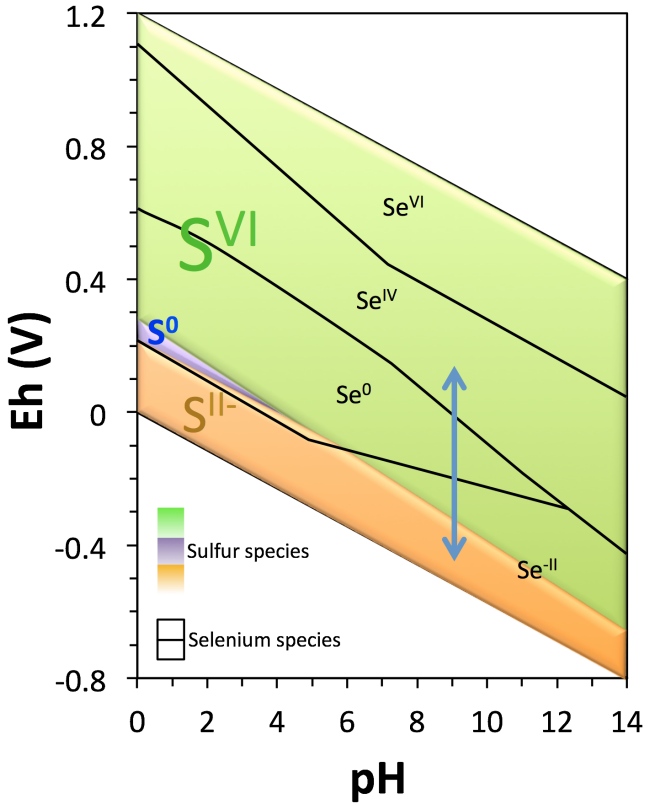


**Figure 1** Combined S and Se Pourbaix diagrams for 25 °C and 1 bar pressure. Large arrow shows required minimum redox variation for selenite-selenide transition that requires higher redox variation than the sulfide-sulfate transition for slab fluids with pH of up to 9 in subduction zones (Galvez *et al.*, 2016).

Chen *et al.*, 2019; Urann *et al.*, 2020). The Raspas complex thus represents an exceptional example of a rather complete sequence of an oceanic lithosphere that has experienced long lived oceanic subduction and is not compromised by potential effects of subsequent continent-continent collision.

## Samples

The samples analysed here comprise seven eclogites, one metapelite, and three high pressure serpentinites from the Raspas Complex (Supplementary Information Tables S-1 and S-2). They have been thoroughly investigated for their petrology and all samples record evidence for hydration prior to subduction, but have been mostly selected to avoid any detectable exhumation related overprint (John *et al.*, 2010; Halama *et al.*, 2011; Herms *et al.*, 2012). A comprehensive major, trace element, Rb-Sr, Sm-Nd, Lu-Hf geochronological and stable Mo-Li-N-Tl isotope dataset is also available (*e.g.*, Halama *et al.*, 2010; John *et al.*, 2010; Chen *et al.*, 2019; Su *et al.*, 2019). We also analysed four serpentinites and gabbros from the deepest Pacific drillcore available (IODP-1256D; Table S-1). We combine this sample set with an average composition of marine sediment from the literature to provide a reliable estimate of subduction input signatures.

## Selenium Isotope Signatures of Prograde Metamorphic Rocks

Compared to the relatively small range for mantle samples including average MORB with $\delta^{82/76}$Se ($\delta^{82/76}Se = [(^{82}Se/^{76}Se)_{sample}/(^{82}Se/^{76}Se)_{NIST3149} - 1] \times 1000$) of −0.16 ± 0.12 ‰ (2 s.d.; Yierpan *et al.*, 2019), peridotites of −0.03 ± 0.07 ‰ (Varas-Reus *et al.*, 2019) and the limited variability observed in seawater overprinted altered ocean crust (AOC) with $\delta^{82/76}$Se of −0.35 to −0.07 ‰ (Pacific drillcore samples; Table S-1), eclogites record a large variation in $\delta^{82/76}$Se from −1.89 to +0.48 ‰ (Fig. 2; see Supplementary Information for analytical methods). High pressure serpentinites and metapelites show $\delta^{82/76}$Se of +0.07 to +0.39 ‰, overlapping with the highest $\delta^{82/76}$Se values of eclogites. $\delta^{82/76}$Se values show no systematic variations with Se concentrations (6 to 106 ng·g$^{-1}$) and samples with the highest Se contents span the entire Se isotope range of the dataset. High pressure serpentinites show highest relative abundances of fluid mobile elements like Pb, Rb, Cs (Fig. 2a–c) or Ba, Li (not shown) when plotted as ratios with fluid immobile Ce as the denominator (see also Fig. S-1). All eclogites show a trend towards lower $\delta^{82/76}$Se with decreasing Pb/Ce, Rb/Ce and Cs/Ce (Fig. 2a). Eclogites with the lowest $\delta^{82/76}$Se sample also display the lowest $\delta^{98/95}$Mo (Fig. 2d; Mo data by Chen *et al.*, 2019) but two samples with only intermediate $\delta^{98/95}$Mo show the most positive $\delta^{82/76}$Se. Additionally, eclogites with the lowest $\delta^{82/76}$Se show the highest contents of Cu, Cl, Sc (Fig. 3) and N as well as the smallest $\delta^{15}$N range (Fig. S-2; Halama *et al.*, 2010; Urann *et al.*, 2020). No correlations between $\delta^{82/76}$Se and Li or Tl isotopes are observed (Fig. S-2).

## Selenium Isotope Vestige of Slab Dehydration

Selenium isotopes do not fractionate significantly during melting, fractional crystallisation and metasomatism (Varas-Reus *et al.*, 2019; Yierpan *et al.*, 2019). The $\delta^{82/76}$Se range of eclogites and clear positive covariations of $\delta^{82/76}$Se with several fluid proxies (Fig. 2a–c) therefore suggest a non-magmatic origin of these signatures. Moreover, since the eclogite facies mineral assemblages show no evidence of subsequent retrograde greenschist facies overprint (except for one sample selected here; John *et al.*, 2010; Herms *et al.*, 2012), the $\delta^{82/76}$Se and their preserved fluid related trends must be attributed to dehydration processes prior to exhumation. Analysed AOC extends to slightly lower $\delta^{82/76}$Se and the high pressure serpentinites to slightly higher $\delta^{82/76}$Se than mantle, while both assemblages maintain a much narrower range than the eclogites. Light S isotope compositions of pyrite in subducted rocks from SW Tianshan, China could be traced back to the alteration of oceanic crust and subsequent, fluid driven sulfide recrystallisation events with prograde metamorphism (Su *et al.*, 2019). Such abyssal seawater-rock interaction therefore also explains the low average $\delta^{82/76}$Se in our AOC, due to scavenging related partial reduction of preferentially light Se isotopes in an entirely oxic water column (*e.g.*, Johnson, 2004). In conclusion, following subduction of AOC with moderately low $\delta^{82/76}$Se, higher $\delta^{82/76}$Se of the high pressure serpentinites as well as the large $\delta^{82/76}$Se range of the eclogites are best explained by slab dehydration during prograde metamorphism at the blueschist-eclogite transition.

## Role of Oxidised Slab Fluids

In fluid-solid systems, isotopes of Se are significantly fractionated during partial reduction of oxidised $Se^{6+}$ to $Se^{4+}$ or further to $Se^{2-}$ (Johnson, 2004). Sulfides thus preferentially incorporate isotopically light Se (*e.g.*, König *et al.*, 2019). Even at 25 °C and 1 atm, the transition from $Se^{2-}$ to $Se^{0}$ and $Se^{4+}$ starts at higher redox potential (Eh) and thus require higher $fO_2$ than the sulfide-sulfate transition (Fig. 1). This difference remains with slightly elevated slab fluid pH of up to 9 in subduction zones

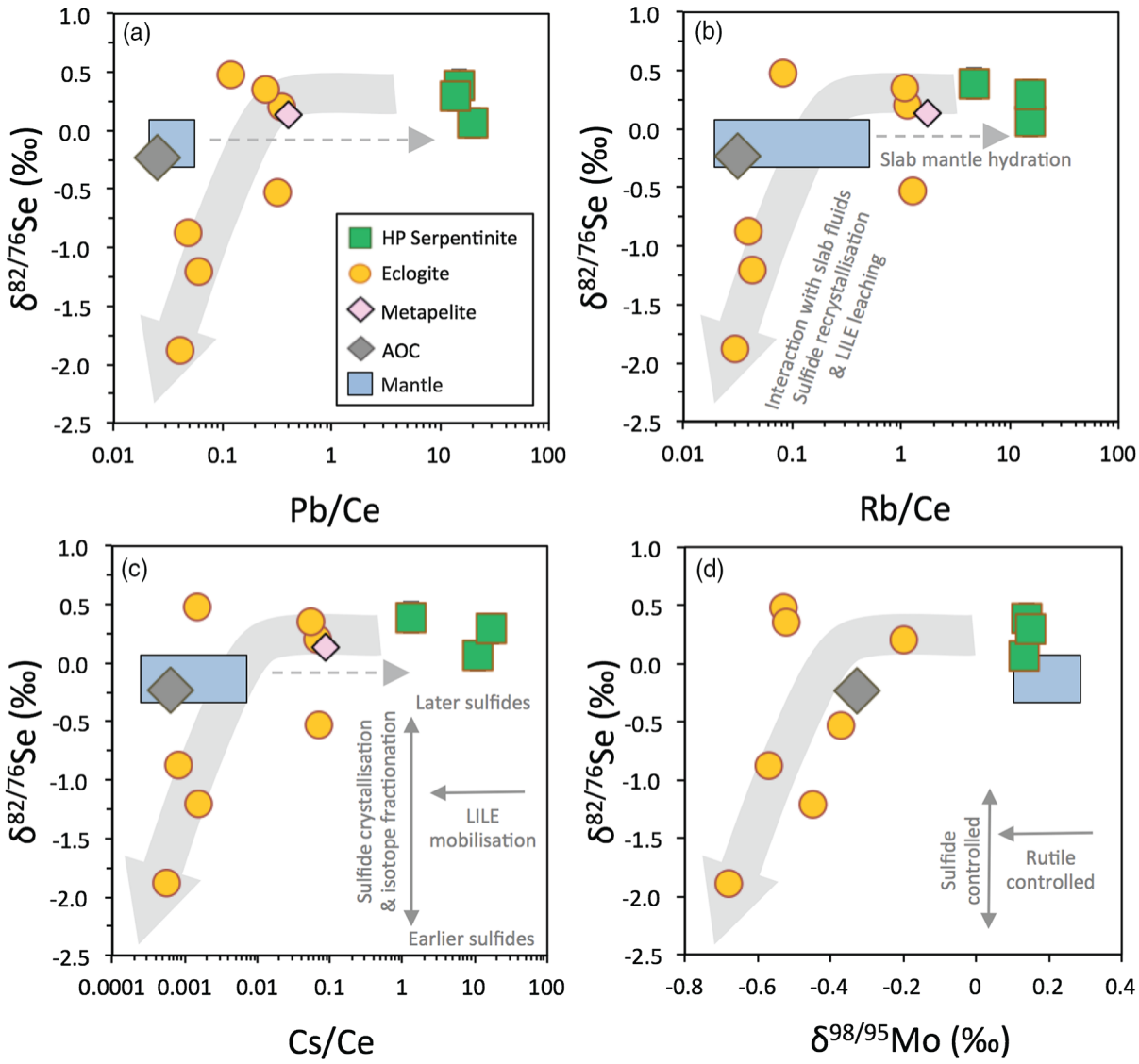


**Figure 2** Selenium isotope composition of Raspas samples and AOC from 1256D *vs.* **(a)** Pb/Ce, **(b)** Rb/Ce, and **(c)** Cs/Ce (Halama *et al.*, 2010; John *et al.*, 2010), and **(d)** $\delta^{98/95}$Mo variation. Mantle includes representative peridotites (Varas-Reus *et al.*, 2019) and MORB (Yierpan *et al.*, 2020). The large grey arrow (Figs. 2, 3) represents our interpretation of the effects of slab mantle dehydration and increasing interaction of subducted crust with slab fluids. The source of Mo is HP serpentinite (Chen *et al.*, 2019), whereas Se is derived mostly from the AOC. As HP serpentinites dehydrate and flush the overlying subducted AOC, rutiles in the subducted crust preferentially retain low $\delta^{98/95}$Mo as the complementary, high $\delta^{98/95}$Mo fluid is removed into the mantle wedge (Freymuth *et al.*, 2015; Chen *et al.*, 2019). Recrystallising, early sulfides preferentially incorporate light Se isotopes and later stage sulfides become isotopically heavier. Repeated sulfide dissolution-recrystallisation produces a spectrum of low and high $\delta^{82/76}$Se in the flushed AOC.

(Galvez *et al.*, 2016). At present, $Se^{6+}/\Sigma Se$ equilibrium values for substantially higher temperatures and pressures are unavailable and therefore the quantification of $fO_2$ from the inferred presence of oxidised Se in slab fluids requires further experimental work. However, such experimentally derived constants exist for $S^{6+}/\Sigma S$ and were previously used to infer a range of slab fluid FMQ of +1.0 to +1.4 at 1.5 GPa from observed sulfate as well as anhydrite saturation in sub-arc mantle peridotites and melt inclusions (Bénard *et al.*, 2018). The sulfate-sulfide transition at conditions relevant to the Raspas eclogite suite at 2 GPa and 600 °C requires *ca.* FMQ +2.5. If significant ΔEh between lower sulfate and selenite stabilities persist at 600 °C and 2 GPa, the occurrence of oxidised Se points to above FMQ +2 for slab fluids involved here. This would agree with previous estimates for slab fluid $fO_2$ above FMQ +2 based on Mo isotope data of Raspas eclogites (Chen *et al.*, 2019). More accurate constraints require experimental work, yet Se isotope data can already be attributed to more pronounced minimum redox variations than those required for stability of oxidised S and even Mo in the subducting slab, as supported by other studies arguing for variably pronounced oxidation potentials of fluids in subduction zones (*e.g.*, Bénard *et al.*, 2018; Chen *et al.*, 2019; Piccoli *et al.*, 2019; Li *et al.*, 2020; Walters *et al.*, 2020).

## Sulfide Dissolution-Recrystallisation

High pressure, intra-slab fluid flow occurs as channelised and in pulses, variably affecting slab mineralogy (*e.g.*, Herms *et al.*, 2012; John *et al.*, 2012; Chen *et al.*, 2019). The lack of systematic covariations between $\delta^{82/76}$Se and other stable isotope signatures of Li, N, and Tl in Raspas eclogites points to different controls on each isotope signature. Kinetically controlled Li isotope fractionation is related to diffusion during fluid-rock interaction

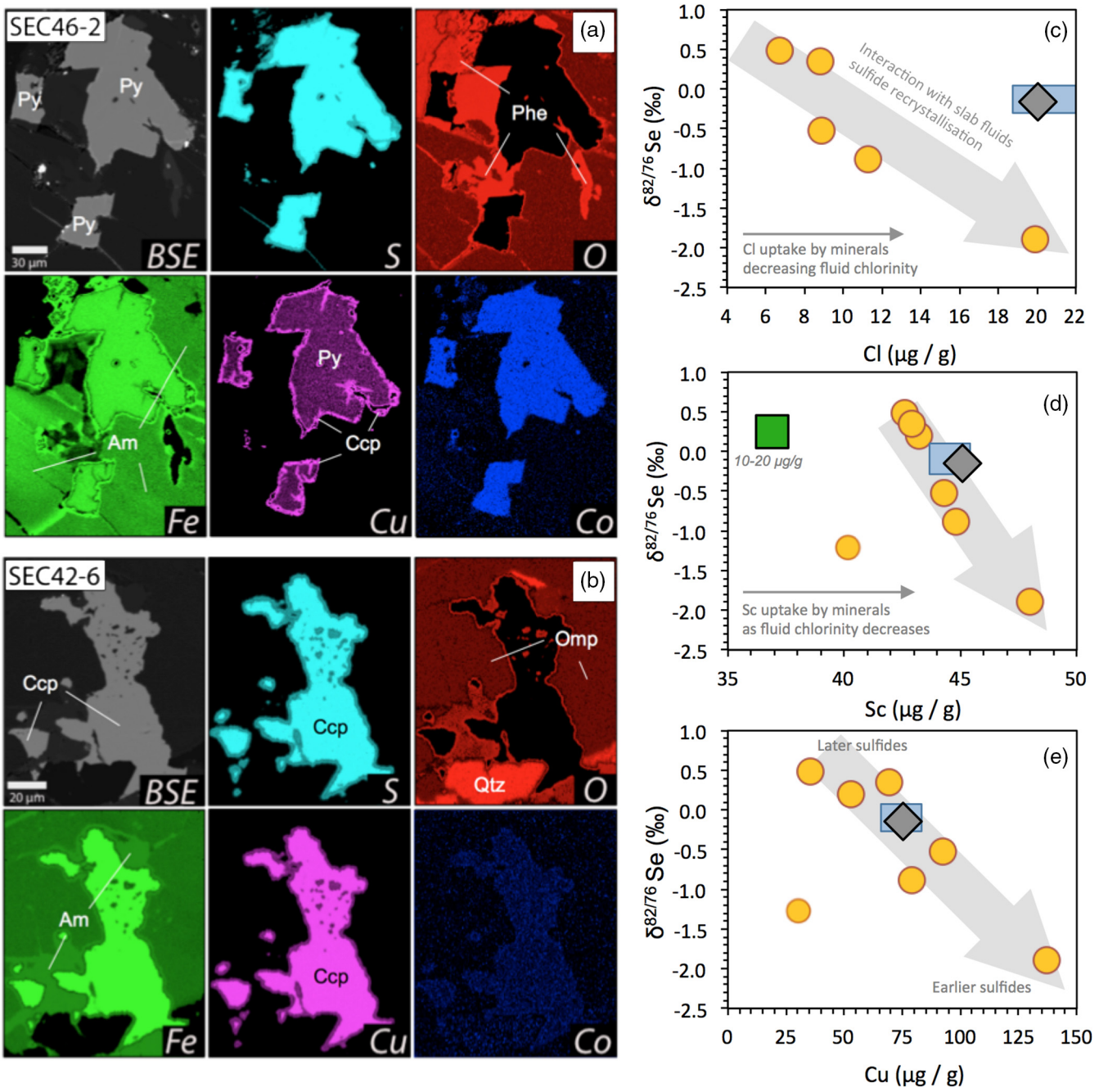


**Figure 3** BSE images and semi-quantitative element mapping of sulfides in Raspas eclogites: **(a)** a partially resorbed Co-bearing pyrite, showing high Cu and Fe contents at the recrystallised chalcopyrite rim and **(b)** an example of a chalcopyrite with a narrow and oxidised rim, indicated by the lower S and Cu contents. Trends of $\delta^{82/76}$Se *vs*. concentrations of **(c)** Cl, **(d)** Sc and **(e)** Cu in prograde eclogites are interpreted to result from this changing fluid-mineral chemistry. Symbols are the same as those used in Figure 2.

(Halama *et al.*, 2011). Lighter N and Tl isotope signatures of Raspas eclogites compared to MORB indicate preservation of low temperature AOC signatures during subduction (Halama *et al.*, 2010; Shu *et al.*, 2019). In contrast to these lithophile element based isotope systems, chalcophile Se substitutes for S in sulfides and witnesses repeated sulfide dissolution-recrystallisation events as fluids pulse through the slab (Evans *et al.*, 2014; Su *et al.*, 2019; Li *et al.*, 2020). This is supported by the mineral assemblages of the eclogites that show sulfides in different stages of dissolution and recrystallisation (Fig. 3a,b) and covariations between $\delta^{82/76}$Se and trace elements (Fig. 3c–e). Eclogite 46-2, for which a partially recrystallised pyrite with highest Co contents and high Cu (chalcopyrite) rims is shown (Fig. 3a), has the lowest bulk $\delta^{82/76}$Se and highest Cl contents (Fig. 3c). This sample also contains abundant apatite, with up to 300 µg·g$^{-1}$ Cl (Urann *et al.*, 2020), suggesting that breakdown of hydrous Cl complexes, possibly cause co-precipitation of cations like Sc that partition into matrix minerals (*e.g.*, Sc into omphacite and garnet, Fig. 3d). This coincides with recrystallisation of sulfides that increase Cu contents in eclogites (Fig. 3a,e). Whereas Mo isotopes in the bulk eclogites record the integrated and unidirectional signature of interaction between fluid and rutile-bearing rocks (Fig. 2d; Chen *et al.*, 2019), $\delta^{82/76}$Se signatures in subducted rocks seem to capture snapshots of repeated and localised sulfide dissolution-recrystallisation effects during highly oxidised, channelised intra-slab fluid flow.

We compared our data to closed system equilibrium and Rayleigh-type fractionation models, which express Se isotope behaviour during partial reduction of Se incorporated into (re)-crystallising sulfides from migrating slab fluids. Sulfides that partly dissolve, recrystallise and dissolve again are neither entirely removed nor fully remixed into the system and hence neither closed nor open system Rayleigh fractionation alone, but a combination of the two can adequately express the entire natural process. This was also previously inferred for such prograde metamorphic conditions for S isotopes (Evans *et al.*, 2014; Supplementary Information and Fig. S-3). As such, the result of repeated sulfide dissolution-recrystallisation cycles during continuous and pulsed fluid flow is the most plausible scenario that generates the $\delta^{82/76}$Se spectrum of eclogites. This encompasses low $\delta^{82/76}$Se for early stage, only partially re-dissolved sulfides and high values for late stage and/or significantly reworked, *i.e.* re-dissolved sulfides (Figs. 2, 3, S-3).

## Implications for the Se Subduction Cycle

Our Se data can be reconciled with a repetitive cycle of sulfide dissolution and recrystallisation during oxidising fluid flow through the subducted AOC as previously suggested for S (*e.g.*, Evans *et al.*, 2014; Su *et al.*, 2019). Small scale Se isotope heterogeneities are however likely re-homogenised at the slab scale with continuous sulfide reworking (see Graphical Abstract). We therefore speculate that any significant volume of Se, and by analogy also S, that ultimately crosses the slab-mantle wedge zone into the sub-arc mantle might not be isotopically distinct from an initial subduction input. In other words, considering the big picture mass balance, slab dehydration may affect the mass fraction of Se without necessarily affecting its isotope signature. Preservation of the overall isotope signature of the slab, which is further subducted into the deeper mantle, is able to explain high $\delta^{82/76}$Se of plume-related lavas that trace recycled sedimentary components subducted from a redox stratified Proterozoic ocean (Yierpan *et al.*, 2020), as well as low $\delta^{82/76}$Se of Mariana arc lavas that include recycled materials subducted from a fully oxygenated modern ocean (Kurzawa *et al.*, 2019).

## Acknowledgements

SK acknowledges ERC Starting Grant O2RIGIN (636808). M. Liesegang is thanked for EPMA support and IODP for the drillcore samples. Helpful comments by two reviewers and particularly editor H. Marschall significantly improved this contribution.

*Editor: Horst R. Marschall*

## Additional Information

**Supplementary Information** accompanies this letter at https://www.geochemicalperspectivesletters.org/article2110.

© 2021 The Authors. This work is distributed under the Creative Commons Attribution Non-Commercial No-Derivatives 4.0 License, which permits unrestricted distribution provided the original author and source are credited. The material may not be adapted (remixed, transformed or built upon) or used for commercial purposes without written permission from the author. Additional information is available at https://www.geochemicalperspectivesletters.org/copyright-and-permissions.

**Cite this letter as:** König, S., Rosca, C., Kurzawa, T., Varas-Reus, M.I., Dragovic, B., Schoenberg, R., John, T. (2021) Selenium isotope evidence for pulsed flow of oxidative slab fluids. *Geochem. Persp. Let.* 17, 27–32.

## References

Bénard, A., Klimm, K., Woodland, A.B., Arculus, R.J., Wilke, M., Botcharnikov, R.E., Shimizu, N., Nebel, O., Rivard, C., Ionov, D.A. (2018) Oxidising agents in sub-arc mantle melts link slab devolatilisation and arc magmas. *Nature Communications* 9, 3500.

Chen, S., Hin, R.C., John, T., Brooker, R., Bryan, B., Niu, Y., Elliott, T. (2019) Molybdenum systematics of subducted crust record reactive fluid flow from underlying slab serpentine dehydration. *Nature Communications* 10, 4773.

Evans, K.A., Tomkins, A.G., Cliff, J. Fiorentini, M.L. (2014) Insights into subduction zone sulfur recycling from isotopic analysis of eclogite-hosted sulphides. *Chemical Geology* 365, 1–19.

Freymuth, H., Vils, F., Willbold, M., Taylor, R.N., Elliott, T. (2015) Molybdenum mobility and isotopic fractionation during subduction at the Mariana arc. *Earth and Planetary Science Letters* 432, 176–186.

Galvez, M.E., Connolly, J.A.D., Manning, C.E. (2016) Implications for metal and volatile cycles from the pH of subduction zone fluids. *Nature* 539, 420–424.

Halama, R., Bebout, G.E., John, T., Schenk, V. (2010) Nitrogen recycling in subducted oceanic lithosphere: The record in high- and ultrahigh-pressure metabasaltic rocks. *Geochimica et Cosmochimica Acta* 74, 1636–1652.

Halama, R., John, T., Herms, P., Hauff, F., Schenk, V. (2011) A stable (Li, O) and radiogenic (Sr, Nd) isotope perspective on metasomatic processes in a subducting slab. *Chemical Geology* 281, 151–166.

Herms, P., John, T., Bakker, R.J., Schenk, V. (2012) Evidence for channelized external fluid flow and element transfer in subducting slabs (Raspas Complex, Ecuador). *Chemical Geology* 310-311, 79–96.

John, T., Scherer, E.E., Schenk, V., Herms, P., Halama, R., Garbe-Schonberg, D. (2010) Subducted seamounts in an eclogite-facies ophiolite sequence: the Andean Raspas Complex, SW Ecuador. *Contributions to Mineralogy and Petrology* 159, 265–284.

John, T., Gussone, N., Podladchikov, Y.Y., Bebout, G.E., Dohmen, R., Halama, R., Klemd, R., Magna, T., Seitz, H.-M. (2012) Volcanic arcs fed by rapid pulsed fluid flow through subducting slabs. *Nature Geoscience* 5, 489–492.

Johnson, T.M. (2004) A review of mass-dependent fractionation of selenium isotopes and implications for other heavy stable isotopes. *Chemical Geology* 204, 201–214.

König, S., Eickmann, B., Zack, T., Yierpan, A., Wille, M., Taubald, H., Schoenberg, R. (2019) Redox induced sulfur-selenium isotope decoupling recorded in pyrite. *Geochimica et Cosmochimica Acta* 244, 24–39.

Kurzawa, T., König, S., Alt, J.C., Yierpan, A., Schoenberg, R. (2019) The role of subduction recycling on the selenium isotope signature of the mantle: Constraints from Mariana arc lavas. *Chemical Geology* 513, 239–249.

Lee, C.-T., Luffi, A.P., Chin, E.J., Bouchet, R., Dasgupta, R., Morton, D.M., Le Roux, V., Yin, Q.-Z., Jin, D. (2012) Copper systematics in arc magmas and implications for crust-mantle differentiation. *Science* 336, 64–68.

Li, J.-L., Schwarzenbach, E.M., John, T., Ague, J.J., Huang, F., Gao, J., Klemd, R., Whitehouse, M.J., Wang, X.-S. (2020) Uncovering and quantifying the subduction zone sulfur cycle from the slab perspective. *Nature Communications* 11, 514.

Piccoli, F., Hermann, J., Pettke, T., Connolly, J.A.D., Kempf, E.D., Vieira Duarte, J.F. (2019) Subducting serpentinites release reduced, not oxidized, aqueous fluids. *Scientific Reports* 9, 19573.

Pons, M.L., Debret, B., Bouilhol, P., Delacour, A., Williams, H. (2016) Zinc isotope evidence for sulfate-rich fluid transfer across subduction zones. *Nature Communications* 7, 13794.

Shu, Y., Nielsen, S.G., Marschall, H.R., John, T., Blusztajn, J., Auro, M. (2019) Closing the loop: subducted eclogites match thallium isotope compositions of ocean island basalts. *Geochimica et Cosmochimica Acta* 250, 130–148.

Su, W., Schwarzenbach, E., Chen, L., Li, Y., John, T., Gao, J., Chen, F., Hu, X. (2019) Sulfur isotope compositions of pyrite from high-pressure metamorphic rocks and related veins (SW Tianshan, China): Implications for the sulfur cycle in subduction zones. *Lithos* 348-349, 105212.

Tollan, P., Hermann, J. (2019) Arc magmas oxidized by water dissociation and hydrogen incorporation in orthopyroxene. *Nature Geoscience* 12, 667–671.

Urann, B.M., Le Roux, V., John, T., Beaudoin, G.M., Barnes, J.D. (2020) The distribution and abundance of halogens in eclogites: An in situ SIMS perspective of the Raspas Complex (Ecuador). *American Mineralogist* 105, 307–318.

Varas-Reus, M.I., König, S., Yierpan, A., Lorand, J.-P., Schoenberg, R. (2019) Selenium isotopes as tracers of a late volatile contribution to Earth from the outer Solar System. *Nature Geoscience* 12, 779–782.

Walters, J.B., Cruz-Uribe, A.M., Marschall, H.R. (2020) Sulfur loss from subducted altered oceanic crust and implications for mantle oxidation. *Geochemical Perspectives Letters* 13, 36–41.

Yierpan, A., König, S., Labidi, J., Schoenberg, R. (2019) Selenium isotope and S-Se-Te elemental systematics along the Pacific-Antarctic ridge: Role of mantle processes. *Geochimica et Cosmochimica Acta* 249, 199–224.

Yierpan, A., König, S., Labidi, J., Schoenberg, R. (2020) Recycled selenium in hot spot-influenced lavas records ocean-atmosphere oxygenation. *Science Advances* 6, eabb6179.

Geochemical Perspectives Letters

© 2021 The Authors
Published by the European Association of Geochemistry

# Selenium isotope evidence for pulsed flow of oxidative slab fluids

**S. König, C. Rosca, T. Kurzawa, M.I. Varas-Reus, B. Dragovic, R. Schoenberg, T. John**

## Supplementary Information

The Supplementary Information includes:

- Analytical Methods
- Figures S-1 and S-2
- Sulfide Dissolution-recrystallisation: Modelling Parameters
- Sulfide Dissolution-recrystallisation: Evaluation of Model Applied to our Data
- Figure S-3
- Tables S-1 to S-5
- Supplementary Information References

## *Analytical Methods*

All analyses were performed in the ISO-5 (US FED standards class 100) clean-room facilities of the Isotope Geochemistry Group at the University of Tuebingen, Germany. De-ionised water was further purified to 18.2 MΩ·cm (at 25 °C) using a Merck Millipore Milli-QTM system. Sample preparation and measurements involved usage of reagents that were distilled from MERCK Millipore Emsure$^{TM}$ grade $HNO_3$ (65 %) and HCl (37 %) using Savillex$^{TM}$ DST-1000 Acid Purification Systems. When necessary, reagents were diluted to required molarities to ±0.03 mol·L$^{-1}$ (by titration).

All samples were ground below 25 µm particle size to provide powder material, which can be effectively dissolved via hotplate PFA beaker digestion and, if not fully dissolved in the case of small garnet fragments, provide sufficient surface for near-quantitative dissolution of sulfides as dominant Se hosts. This was also demonstrated by comparison of Se concentrations additionally obtained for selected samples via bomb and high-pressure-asher (HPA) digestion (SEC 47-1, SEC 50-1, and USGS BCR-2; Tables S-3 and S-4) techniques as well as multiple hotplate PFA beaker digestions of some samples. Pressure bomb digestions yield Se concentrations slightly lower than concentrations obtained from table-top digestions. This can be explained through moderate loss of volatile Se during the polytetrafluoroethylene (PTFE) bomb digestion. HPA digestion of sample SEC 50-1 yielded a Se concentration of 87 ng·g$^{-1}$, which is similar to concentrations obtained from table top digestions. These results strongly suggest that quantitative dissolution of Se from sample powders, which still might contain small <25 µm garnet fragments is achieved. A general pre-determination of Se concentrations from a minor sample powder aliquot identifies precise

double spike amounts to be added to the main powder aliquot for an ideal spike-sample ratio of ~1:1 for Se isotope analyses (Kurzawa *et al*., 2017; Yierpan *et al*., 2018). In brief, ca. 20 mg sample powder material is mixed with an equal amount of $^{74}$Se–$^{77}$Se double spike. The sample-spike mix is digested using an acid mixture of 5:1 (v/v) conc. HF : conc. $HNO_3$ in closed beakers at 85 °C. Following a dry-down at 65 °C and chloride conversion (see Yierpan *et al*., 2018) Fe is removed by means of anion exchange chromatography. For Se concentration analyses on the iCAP Qs, Fe-free cuts were diluted to 0.5-1 ng·mL$^{-1}$ Se and following the protocol by Yierpan *et al*. (2018).

For Se isotope analyses we followed the protocol by Yierpan *et al*. (2018). For this, sample material equivalent to ca. 30 ng Se is mixed with an adequate amount of $^{74}$Se-$^{77}$Se double spike (1:1; sample Se : double spike Se) and digested in conc. HF : $HNO_3$ 5:1 (v/v) in closed beakers on a hotplate at 85 °C for 48 hours. Selenium is purified from sample solutions in a two-step ion exchange chromatography. In a first column, Fe is eliminated via anion exchange chromatography. This is followed by a cation exchange column to purify the Se cut from the remaining matrix. Selenium isotope compositions were analysed on a ThermoFisher Scientific Neptune$^{Plus}$ MC-ICP-MS by hydride generation and in low resolution mode at the Isotope Geochemistry laboratory, University of Tuebingen. Typical signals on $^{82}$Se (using an amplifier resistor of $10^{11}$ Ω) on a 30 ng·mL$^{-1}$ Se solution with operating parameters similar to those reported by Kurzawa *et al*. (2017) were generally 0.8-0.9 V. Selenium isotopes of samples were determined at similar signal intensities compared to those of standard solutions. For detailed descriptions of analytical techniques employed see Kurzawa *et al*. (2017) and Yierpan *et al*. (2018).

All Se isotope compositions obtained during this study are reported relative to the NIST-3149 Se reference solution (delta-zero-anchor). Measurements of the inter-laboratory standard solution MH-495 yield an average value of $\delta^{82/76}$Se of -3.26 ± 0.09 ‰ (2 s.d., $n$ = 19, 30 ng·mL$^{-1}$ solutions, see Tables S-3), in agreement with previous studies (Kurzawa *et al*., 2017, 2019; Labidi *et al*., 2018; Yierpan *et al*., 2018, 2019). All samples were measured together with the international rock reference material USGS BCR-2, which yield $\delta^{82/76}$Se of 0.14 ± 0.15 ‰ (2 s.d., $n$ = 4) and Se concentration of 78 ng·g$^{-1}$, respectively (Tables S-3). This in agreement with previously published Se concentration and isotope composition (Kurzawa *et al*., 2017; Yierpan *et al*., 2018, 2019). Long-term analytical reproducibility for Se concentration determination is ~3 % (1 s.d.). In most cases, external reproducibility of $\delta^{82/76}$Se for sample materials is <0.13 ‰ (2 s.d.), as derived from multiple digested and analysed sample SEC 43-3 during different measurement sessions (Tables S-3). We chose reproducibility over number of samples ($n$ = 15) and digested critical samples up to four times, amounting to a total of 33 measurements for this study, each from new digestions (Table S-3).

## *Supplementary Figure S-1*

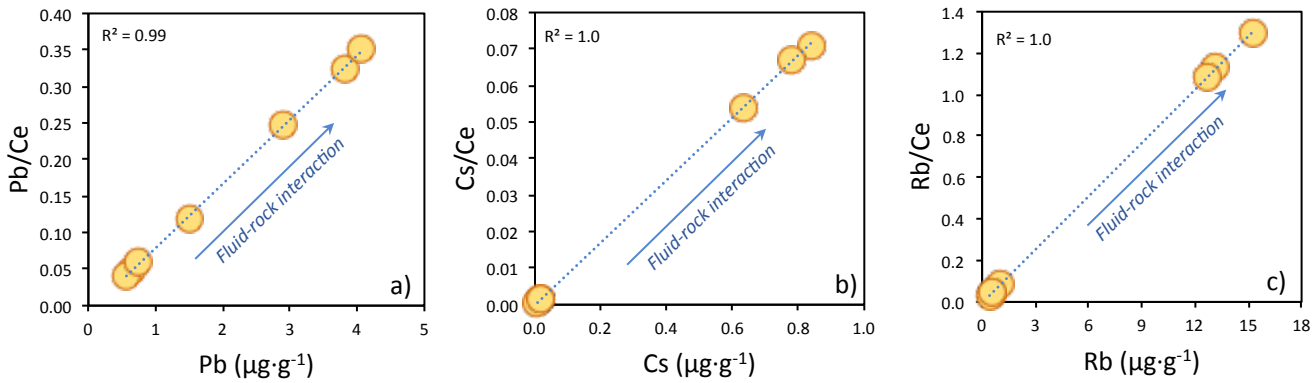


**Figure S-1 (a)** Pb/Ce vs. Pb, **(b)** Cs/Ce vs. Cs and **(c)** Rb/Ce vs. Rb, show the entire range of fluid mobile element concentrations that is independent from igneous processes like melting and differentiation as Ce abundances remain constant. Analytical uncertainties are smaller than symbol sizes.

## *Supplementary Figure S-2*

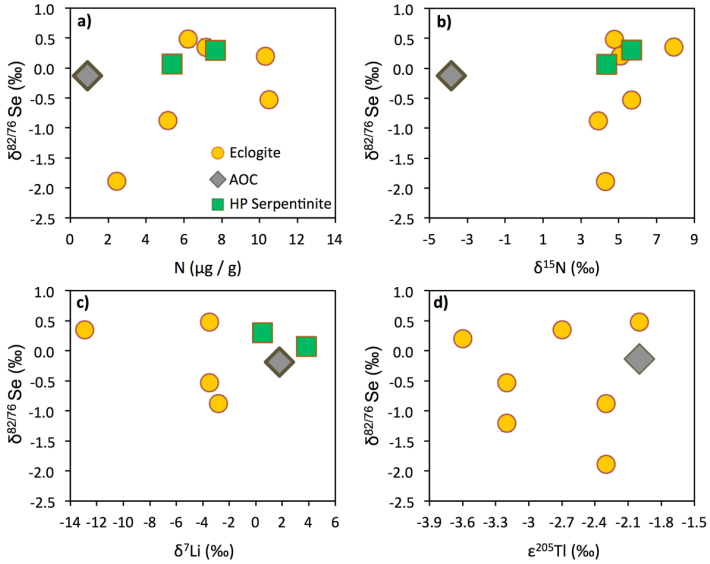


**Figure S-2** Relationship between $\delta^{82/76}$Se and other elemental and isotopic systematics previously studied for these samples. **(a)** N concentrations and **(b)** $\delta^{15}N_{air}$ (both from Halama *et al*., 2010), **(c)** $\delta^{7}$Li (Halama *et al*., 2011), and **(d)** $\varepsilon^{205}$Tl (Shu *et al*., 2019) respectively in eclogites (orange filled circles), serpentinised peridotites (green filled squares) from the Raspas complex, as well as MORB for comparison (grey filled diamond). Error bars for Se isotope ratios are smaller than symbol size.

## *Sulfide Dissolution-recrystallisation: Modelling Parameters*

The relationships between $\delta^{82/76}$Se (‰) of the reactant remaining in the source (*i.e.* progressive devolatilization) and the composition of the evolving sulfides (orange curves) and fluid (blue curves) was calculated with closed-system equilibrium and Rayleigh fractionation models (Fig. S-2). Due to unavailable fractionation factors for Se isotopes at conditions in subduction zones (T = 600-300 °C) a first approximation based on the data from this study was made. The Se isotope composition of the input was set to be represented by the average deepest oceanic crust composition at IODP 1256D ($\delta^{82/76}Se_{input}$ = -0.23 ‰). Note that this value is slightly lighter than the $\delta^{82/76}$Se of the mantle ranging between 0 and -0.15 ‰ (Varas-Reus *et al*., 2019; Yierpan *et al*., 2019). The composition of the eclogite sample SEC 46-2, displaying least fluid amount (Pb/Ce = 0.04 or Ce/Pb = 25) and lightest Se isotope value was used as the fluid-poorest end-member ($\delta^{82/76}Se_{sulfides}$ = -2 ‰), resulting in a $\alpha_{1\ secondary\ sulfides\ -\ fluid}$ = 0.9980. Because even this lightest sample (where Se is mainly hosted by sulfides) is likely influenced by a small amount of fluid (John *et al*., 2010), we calculated a second scenario ($\alpha_2$) with $\alpha_{2\ secondary\ sulfides\ -\ fluid}$ = 0.9960 for comparison. Figure S-2 shows the results of all conducted models. To put the individual data of the Raspas samples in the context of the models a – c, we calculated the relative fluid amount by weighted means based on Pb/Ce values of the samples. For this, the eclogite SEC 46-2 was chosen as minimum end-member because it has the lowest $\delta^{82/76}$Se, shows the least relative fluid amount (*e.g.*, lowest Pb/Ce) and has the majority of Se stored in residual sulfides (highest Cu; see also Figs. 2 and 4a in the main manuscript). A $\delta^{82/76}$Se composition of -1.89 ‰ can thus be attributed to a weighted mix between ca. 70 % of Se hosted by precipitated sulfides and ca. 30 % Se hosted by fluid. All other samples were calculated according to this sample. For the models involving Se concentrations (Figure S-2e-h), modelled fluid and precipitated sulfide lines were calculated from an initial concentration of 196 ng·g$^{-1}$, based on average concentration in the IODP 1256D samples. Selenium IC and concentrations of Raspas samples are presented along with the models without applying any correction. Altogether, we note that calculations conducted with the two different $\alpha_{secondary\ sulfides\ -\ fluid}$ yield relatively similar results. The Se isotope composition of the samples with least fluid amount (*i.e.* majority of Se hosted in sulfides) can be best explained by a kinetic fractionation, while those approaching the input composition are best explained by an equilibrium effect. The Se isotope systematics in Raspas samples are therefore best explained by a mix between equilibrium and kinetic effects. Symbols for the samples are as in Fig. 2a (main manuscript). Error bars are smaller than symbols.

## *Sulfide Dissolution-recrystallisation: Evaluation of Model Applied to our Data*

Based on the different calculated models (see above) that account for the relative amount of fluid in the samples and Se concentrations, the following scenario is proposed: Serpentinised mantle-derived fluids first dissolve slab crust-hosted sulfides from which oxidised Se species are mobilised. Subsequent reduction of Se then occurs during re-incorporation into re-crystallising sulfides. Preferential re-incorporation of reduced and isotopically light Se in sulfides from the migrating fluids in turn make these fluids isotopically heavier. This produces both isotopically lighter residual- and heavier fluid signatures with increasing degree of fluid-rock interaction. On the other hand, additional fluid pulses with isotopically heavier Se-bearing fluids will again re-dissolve formerly recrystallised, isotopically lighter Se-bearing sulfides on their ascending trajectory. This hypothesis is supported by our Se isotope data, which is best explained by a mix between a Rayleigh-type open system fractionation for the samples displaying the lightest isotope signature, and a closed-system equilibrium applicable for the samples reaching "input" values. This fluid-related dissolution and re-precipitation is consistent with previously observed trace element and $\delta^{34}S$ zoning in pyrite grains within eclogites and eclogite-facies fossilised fluid-flow structures (*i.e.* vein systems) indicating repeated cycles of sulfide dissolution-recrystallisation (Su *et al*., 2019; Li *et al*., 2020). In some cases, this was observed in combination with chlorine-rich slab fluids (Evans *et al*., 2014). As such, the relatively large Se isotopic range in our suite, which is produced during prograde metamorphism can most likely be traced back to different stages of sulfide precipitation-dissolution during episodic slab flushing pulses. Our Se isotope data however provide an additional line of evidence pointing to the link between higher redox variations than previously derived from S systematics and offer a new perspective to constrain the role of oxidized fluids in chalcophile element cycling in subduction zones.

## *Supplementary Figure S-3*

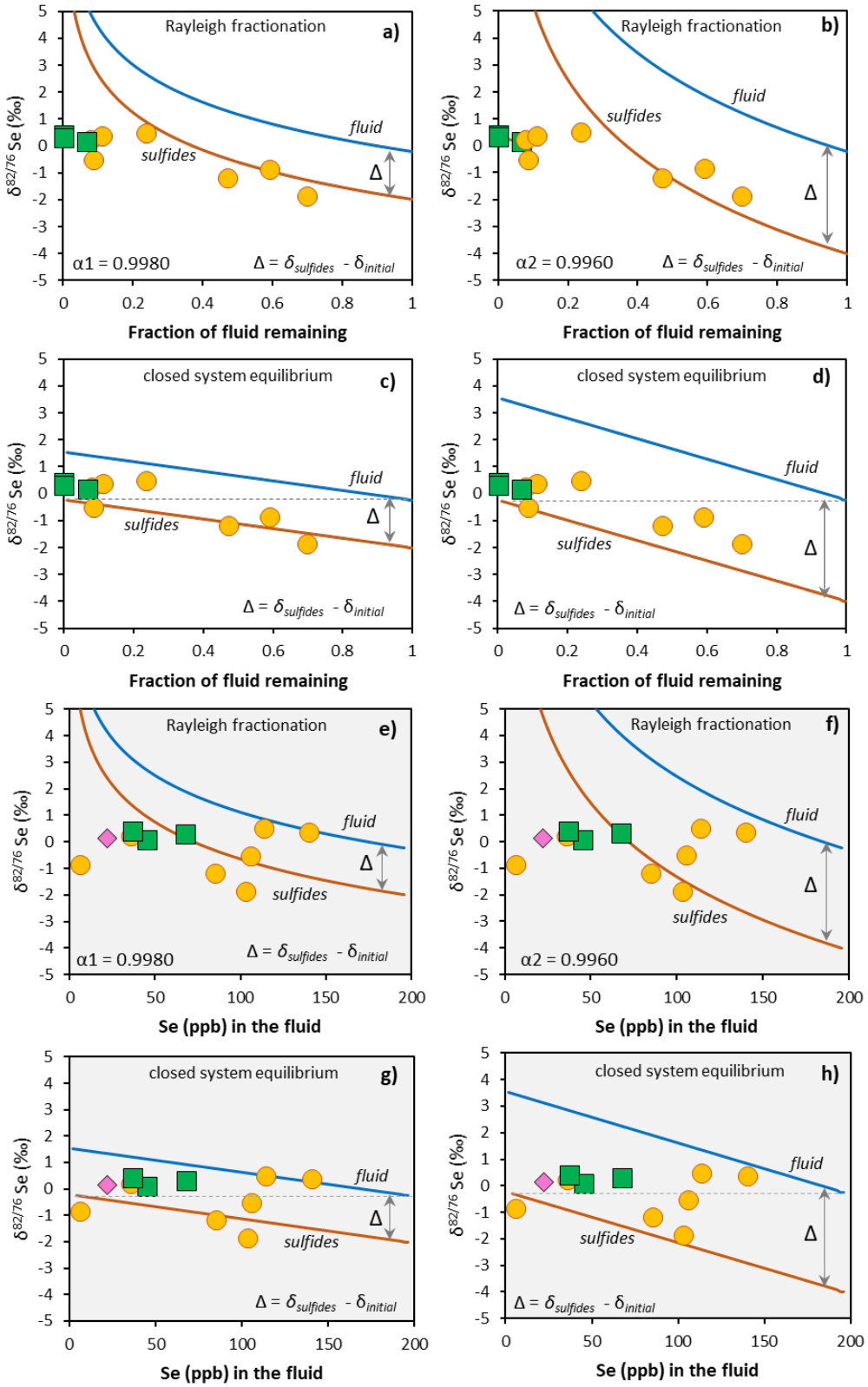


**Figure S-3** Calculated $\delta^{82/76}$Se (‰) relationships between sulfide precipitation (orange lines) from a fluid and the corresponding fluid (blue lines) evolution using: **(c)**, **(d)**, **(g)**, **(h)** closed system fractionation (equilibrium) and **(a)**, **(b)**, **(e)**, **(f)** kinetic fractionation described by Rayleigh dynamics. Models are calculated with two hypothetical fractionation factors ($\alpha$ = 0.9980 in **(a)**, **(c)**, **(e)**, **(g)**; and $\alpha$ = 0.9960 in **(b)**, **(d)**, **(f)**, **(h)**) as described in detail in the text above. Model calculations conducted using Se concentrations were made by adopting an average value based on the IODP-1256D sample compositions.

# *Supplementary Tables*

**Table S-1** Average Se concentrations and Se isotope compositions of eclogites from the Raspas complex, serpentinised peridotites, metapelite and AOC from IODP1256D - Cocos Plate. Individual data listed in Table S-3 HP = high-pressure; serp. = serpentinised, ret. = retrogressed to a minor degree. *Internal precision on a sample run (over 40 cycles) is reported as 2 standard error (2 s.e.).

| Sample name | Rock type | Se ng $g^{-1}$ | $\delta^{82/76}$Se (‰) | Average 2 s.e. (‰)* |
|---|---|---|---|---|
| SEC 43-1 | Eclogite | 114 | 0.48 | *0.08* |
| SEC 43-3 | Eclogite | 106 | -0.53 | *0.06* |
| SEC 44-1 | Eclogite | 36 | 0.2 | *0.1* |
| SEC 46-1 | Eclogite | 6.4 | -0.88 | *0.11* |
| SEC 46-2 | Eclogite | 104 | -1.89 | *0.09* |
| SEC 47-1 | Eclogite | 141 | 0.35 | *0.07* |
| SEC 50-1 | ret. Eclogite | 85.3 | -1.21 | *0.06* |
| SEC 35-2 | HP serpentinite | 45.5 | 0.07 | *0.06* |
| SEC 36-2 | HP serpentinite | 37 | 0.39 | *0.1* |
| SEC 40-1 | HP serpentinite | 68 | 0.3 | *0.08* |
| SEC 45-3 | metapelite | 22 | 0.14 | *0.08* |
| IODP1256D-309-75R1 | serp. Basalt | 170 | -0.35 | *0.07* |
| IODP1256D-309-132R1 | serp. Basalt | 182 | -0.07 | *0.06* |
| IODP1256D-312-216R1 | gabbro | 204 | -0.35 | *0.06* |
| IODP1256D-312-232R1 | gabbro | 230 | -0.17 | *0.06* |

**Table S-2** Major and trace element data of eclogites, serpentinised peridotites, metapelite and AOC from IODP1256D - Cocos Plate. Data from Halama *et al.* (2010) and John *et al.* (2010). Italic numbers of metapelite refer to average concentrations and element ratios of metasediments from the Franciscan Complex and the Western Baja Terrane; data from Sadofsky and Bebout (2003). HP Serp. = high-pressure serpentinite, serp. Bas. = serpentinised basalt, ret. = retrogressed to a minor degree.

| Sample | SEC 43-1 | SEC 43-3 | SEC 44-1 | SEC 46-1 | SEC 46-2 | SEC 47-1 | SEC 50-1 | SEC 35-2 | SEC 36-2 | SEC 40-1 | SEC 45-3 | 309-75R1 | 309-132R1 | 312-216R1 | 312-232R1 |
|---|---|---|---|---|---|---|---|---|---|---|---|---|---|---|---|
| Rock type | Eclogite | Eclogite | Eclogite | Eclogite | Eclogite | Eclogite | ret. Ecl. | HP Serp. | HP Serp. | HP Serp. | Meta-pelite | serp. Bas. | serp. Bas. | Gabbro | Gabbro |
| *Major oxides (wt. %)* | | | | | | | | | | | | | | | |
| $SiO_2$ | 47.92 | 50.17 | 48.67 | 44.08 | 44.88 | 47.49 | 49.57 | 40.49 | 40.24 | 41.54 | | - | - | - | - |
| $TiO_2$ | 1.79 | 1.86 | 1.91 | 1.87 | 2.00 | 1.94 | 1.88 | 0.05 | 0.04 | 0.03 | | - | - | - | - |
| $Al_2O_3$ | 14.67 | 11.97 | 12.37 | 13.93 | 12.39 | 12.48 | 11.97 | 2.37 | 1.34 | 1.69 | | - | - | - | - |
| $Fe_2O_3$ | 13.04 | 13.3 | 13.75 | 15.48 | 13.77 | 13.87 | 13.30 | 8.02 | 8.23 | 8.64 | | - | - | - | - |
| MnO | 0.19 | 0.23 | 0.19 | 0.24 | 0.21 | 0.23 | 0.19 | 0.12 | 0.12 | 0.13 | | - | - | - | - |
| MgO | 6.46 | 6.65 | 6.00 | 10.09 | 8.72 | 6.01 | 6.72 | 37.26 | 40.43 | 40.75 | | - | - | - | - |
| CaO | 11.1 | 10.67 | 10.84 | 10.87 | 13.41 | 11.15 | 10.48 | 2.48 | 0.28 | 1.85 | | - | - | - | - |
| $Na_2O$ | 3.09 | 3.02 | 3.02 | 1.69 | 2.30 | 2.77 | 3.04 | 0.07 | 0.00 | 0.25 | | - | - | - | - |
| $K_2O$ | 0.53 | 0.07 | 0.48 | 0.16 | 0.11 | 0.51 | 0.07 | 0.01 | 0.00 | 0.01 | | - | - | - | - |
| $P_2O_5$ | 0.13 | 0.17 | 0.16 | 0.11 | 0.74 | 0.17 | 0.17 | 0.01 | 0.01 | 0.00 | | - | - | - | - |
| LOI | 0.57 | 0.42 | 0 | 0.45 | 0 | 0.37 | 0.81 | 10.01 | 10.06 | 5.67 | | - | - | - | - |
| Total | 99.49 | 100.45 | 99.86 | 99.75 | 99.63 | 99.58 | 99.85 | 100.89 | 100.75 | 100.56 | | - | - | - | - |
| *Trace elements ($\mu g \cdot g^{-1}$)* | | | | | | | | | | | | | | | |
| Li | 48.5 | 13.8 | 51.4 | 11.0 | 13.3 | 67.3 | 20.3 | 0.990 | 1.03 | 2.76 | | 4.59 | 3.20 | 1.47 | 2.44 |
| Be | | | | | | | | | | | | 0.347 | 0.346 | 0.250 | 0.317 |
| Sc | 44.3 | 42.6 | 43.2 | 44.8 | 48 | 42.9 | 39.6 | 16.8 | 10.5 | 11.2 | | 8786 | 7187 | 5036 | 7647 |
| V | 376 | 390 | 389 | 362 | 431 | 358 | 329 | 73.6 | 37.1 | 51.1 | | 362 | 310 | 198 | 295 |
| Cr | 214 | 111 | 211 | 253 | 252 | 256 | 144 | 2674 | 2775 | 2344 | | 53.7 | 85.3 | 311 | 472 |
| Co | 45.7 | 40.1 | 45.0 | 51.9 | 37.9 | 45.4 | 38.4 | 104 | 100 | 102 | | 50.3 | 44.8 | 39.8 | 40.4 |
| Ni | 77.5 | 53.0 | 75.9 | 71.2 | 59.1 | 74.2 | 47.0 | 1957 | 2116 | 2125 | | 45.4 | 52.6 | 78.5 | 93.7 |
| Cu | 92.6 | 35.3 | 52.8 | 79.0 | 137 | 69.3 | 32.9 | 4.82 | 2.47 | 20.3 | | 85.2 | 66.5 | 57.7 | 81.3 |
| Zn | 229 | 106 | 218 | 280 | 277 | 143 | 57.4 | 50.3 | 43.0 | 42.3 | | 109 | 89.3 | 37.2 | 39.7 |

**Table S-2** ***cont.***

| Sample | SEC 43-1 | SEC 43-3 | SEC 44-1 | SEC 46-1 | SEC 46-2 | SEC 47-1 | SEC 50-1 | SEC 35-2 | SEC 36-2 | SEC 40-1 | SEC 45-3 | 309-75R1 | 309-132R1 | 312-216R1 | 312-232R1 |
|---|---|---|---|---|---|---|---|---|---|---|---|---|---|---|---|
| Rock type | Eclogite | Eclogite | Eclogite | Eclogite | Eclogite | Eclogite | ret. Ecl. | HP Serp. | HP Serp. | HP Serp. | Meta-pelite | serp. Bas. | serp. Bas. | Gabbro | Gabbro |
| Ga | 19.2 | 18.2 | 18.4 | 13.1 | 10.9 | 19.0 | 16.3 | 2.10 | 1.56 | 1.72 | | 19.0 | 16.2 | 15.2 | 15.7 |
| As | | | | | | | | | | | | 0.188 | 0.196 | 0.133 | 0.163 |
| Rb | 15.3 | 1.06 | 13.1 | 0.530 | 0.420 | 12.7 | 0.54 | 0.215 | 0.071 | 0.200 | *63.1* | 0.084 | 0.186 | 0.388 | 0.210 |
| Sr | 92.5 | 77.0 | 66.8 | 31.6 | 36.8 | 103 | 84.9 | 3.53 | 1.51 | 1.63 | | 84.1 | 72.8 | 96.7 | 93.0 |
| Y | 43.1 | 46.1 | 45.1 | 49.1 | 46.4 | 48 | 50.5 | 1.58 | 0.504 | 0.919 | | 31.7 | 26.1 | 18.4 | 27.5 |
| Zr | 116 | 109 | 110 | 102 | 104 | 109 | 119 | 9.49 | 0.294 | 0.049 | | 73.5 | 64.0 | 12.5 | 21.0 |
| Nb | 2.04 | 2.40 | 2.03 | 2.19 | 4.26 | 2.09 | 1.91 | 0.008 | 0.036 | 0.034 | | 2.26 | 3.35 | 1.33 | 1.94 |
| Mo | 0.13 | | | 0.130 | 0.070 | 0.140 | 0.130 | 0.190 | 0.060 | 0.070 | | 0.184 | 0.231 | 0.166 | 0.118 |
| Cd | | | | | | | | | | | | 0.129 | 0.063 | 0.030 | 0.033 |
| Sn | 0.966 | 0.966 | 0.743 | | | 1.18 | | 0.124 | 0.084 | 0.107 | | 0.306 | 0.688 | 0.458 | 0.575 |
| Sb | 0.32 | 0.150 | 0.210 | 0.200 | 0.100 | 0.480 | 1.20 | 0.140 | 3.09 | 0.030 | | 0.012 | 0.027 | 0.005 | 0.002 |
| Cs | 0.837 | 0.019 | 0.777 | 0.011 | 0.008 | 0.632 | 0.019 | 0.157 | 0.020 | 0.218 | *3.15* | 0.006 | 0.007 | 0.003 | 0.002 |
| Ba | 98.8 | 21.2 | 79.4 | 6.76 | 21.1 | 60.9 | 121 | 4.87 | 3.17 | 1.32 | | 4.81 | 11 | 10 | 8.34 |
| La | 4.09 | 3.75 | 3.70 | 4.08 | 4.40 | 3.71 | 3.72 | 0.004 | 0.016 | 0.006 | | 2.54 | 2.97 | 1.67 | 2.14 |
| Ce | 11.8 | 12.7 | 11.6 | 13.6 | 14.1 | 11.7 | 12.4 | 0.014 | 0.015 | 0.013 | *35.7* | 7.77 | 8.09 | 5.05 | 6.84 |
| Pr | 2.14 | 2.28 | 2.17 | 2.53 | 2.46 | 2.18 | 2.32 | 0.006 | 0.006 | 0.003 | | 1.38 | 1.33 | 0.874 | 1.25 |
| Nd | 11.5 | 12.6 | 11.9 | 13.9 | 12.9 | 12.4 | 12.7 | 0.069 | 0.040 | 0.020 | | 7.66 | 7.15 | 4.79 | 7.18 |
| Sm | 4.03 | 4.38 | 4.23 | 5.11 | 4.28 | 4.54 | 4.62 | 0.067 | 0.019 | 0.024 | | 2.89 | 2.56 | 1.79 | 2.70 |
| Eu | 1.43 | 1.57 | 1.57 | 1.71 | 1.51 | 1.57 | 1.59 | 0.032 | 0.008 | 0.011 | | 1.13 | 1.02 | 0.879 | 1.05 |
| Gd | 5.47 | 5.90 | 5.70 | 6.74 | 5.60 | 6.12 | 6.34 | 0.147 | 0.037 | 0.061 | | 4.32 | 3.69 | 2.61 | 3.99 |
| Tb | 1 | 1.08 | 1.07 | 1.18 | 1.00 | 1.17 | 1.17 | 0.034 | 0.008 | 0.016 | | 0.803 | 0.679 | 0.488 | 0.745 |
| Dy | 6.95 | 7.33 | 7.35 | 7.89 | 6.96 | 7.92 | 8.01 | 0.266 | 0.061 | 0.134 | | 5.43 | 4.53 | 3.28 | 4.90 |
| Ho | 1.49 | 1.58 | 1.56 | 1.66 | 1.55 | 1.69 | 1.71 | 0.062 | 0.017 | 0.035 | | 1.25 | 1.02 | 0.729 | 1.10 |
| Er | 4.26 | 4.59 | 4.48 | 4.74 | 4.52 | 4.83 | 4.89 | 0.186 | 0.055 | 0.110 | | 3.59 | 2.92 | 2.08 | 3.18 |
| Tm | 0.628 | 0.688 | 0.668 | 0.713 | 0.679 | 0.712 | 0.727 | 0.030 | 0.011 | 0.019 | | 0.560 | 0.456 | 0.314 | 0.478 |

**Table S-2** ***cont.***

| Sample | SEC 43-1 | SEC 43-3 | SEC 44-1 | SEC 46-1 | SEC 46-2 | SEC 47-1 | SEC 50-1 | SEC 35-2 | SEC 36-2 | SEC 40-1 | SEC 45-3 | 309-75R1 | 309-132R1 | 312-216R1 | 312-232R1 |
|---|---|---|---|---|---|---|---|---|---|---|---|---|---|---|---|
| Rock type | Eclogite | Eclogite | Eclogite | Eclogite | Eclogite | Eclogite | ret. Ecl. | HP Serp. | HP Serp. | HP Serp. | Meta-pelite | serp. Bas. | serp. Bas. | Gabbro | Gabbro |
| Yb | 4.16 | 4.60 | 4.49 | 4.83 | 4.54 | 4.80 | 4.89 | 0.204 | 0.081 | 0.138 | | 3.59 | 2.92 | 1.98 | 3.00 |
| Lu | 0.6 | 0.674 | 0.654 | 0.723 | 0.678 | 0.709 | 0.73 | 0.031 | 0.015 | 0.022 | | 0.536 | 0.431 | 0.288 | 0.437 |
| Hf | 3.01 | 2.85 | 2.89 | 2.86 | 2.91 | 3.13 | 3.25 | 0.238 | 0.015 | 0.011 | | 2.14 | 1.80 | 0.510 | 0.878 |
| Ta | 0.126 | 0.141 | 0.129 | 0.140 | 0.183 | 0.146 | 0.142 | 0.000 | 0.002 | 0.002 | | 0.145 | 0.206 | 0.086 | 0.118 |
| W | 0.17 | 0.170 | 0.450 | | | 0.300 | | 0.090 | 0.060 | 0.140 | | 0.026 | 0.076 | 0.025 | 0.029 |
| Tl | | | | | | | | | | | | 0.001 | 0.002 | 0.002 | 0.001 |
| Pb | 3.81 | 1.50 | 4.06 | 0.646 | 0.566 | 2.90 | 0.738 | 0.280 | 0.223 | 0.179 | *14.5* | 0.228 | 0.242 | 0.124 | 0.093 |
| Th | 0.206 | 0.208 | 0.146 | 0.131 | 0.170 | 0.138 | 0.137 | 0.001 | 0.001 | 0.001 | | 0.147 | 0.225 | 0.052 | 0.092 |
| U | 0.212 | 0.069 | 0.184 | 0.175 | 0.540 | 0.194 | 0.054 | 0.003 | 0.003 | 0.001 | | 0.089 | 0.072 | 0.014 | 0.019 |

**Table S-3** Individual Se concentrations and Se isotope compositions of eclogites from the Raspas complex, serpentinised peridotites, metapelite and AOC from IODP1256D - Cocos Plate. ┼Internal precision on a sample run (over 40 cycles) is reported as 2 standard error (2 s.e.). ret. = retrogressed to a minor degree. HP = high-pressure serpentinite, External reproducibility (uncertainty, 2 standard deviation) only given when $n > 3$ measurements from new sample digests, HPA = High Pressure Asher™ digestion.

| Sample | Rock type | $\delta^{82/76}$Se (‰) | 2 s.e.┼(‰) | Se (ng·g$^{-1}$) |
|---|---|---|---|---|
| SEC 43-1 | Eclogite | 0.47 | 0.09 | 114 |
| | | 0.48 | 0.07 | 114 |
| | *average* | *0.48* | *0.08* | *114* |
| SEC 43-3 | Eclogite | -0.62 | 0.07 | 107 |
| | | -0.53 | 0.06 | 106 |
| | | -0.51 | 0.05 | 105 |
| | | -0.47 | 0.05 | 106 |
| | *average* | *-0.53* | *0.06* | *106* |
| | *uncertainty (2 s.d.)* | *0.13* | | *1.63* |
| SEC 44-1 | Eclogite | 0.20 | 0.10 | 36 |
| SEC 46-1 | Eclogite | -0.90 | 0.16 | 6.56 |
| | | -0.85 | 0.05 | 6.24 |
| | *average* | *-0.88* | *0.11* | *6.40* |
| SEC 46-2 | Eclogite | -1.81 | 0.09 | 105 |
| | | -1.96 | 0.08 | 102 |
| | *average* | *-1.89* | *0.09* | *104* |
| SEC 47-1 | Eclogite | 0.30 | 0.09 | 144 |
| | | 0.37 | 0.09 | 141 |
| | | 0.40 | 0.06 | 138 |
| | | 0.34 | 0.06 | 139 |
| *(bomb digestion)* | | | | *(128)* |
| | *average* | *0.35* | *0.07* | *141* |
| | *uncertainty (2 s.d.)* | *0.08* | | *5.29* |

**Table S-3** ***cont.***

| Sample | Rock type | $\delta^{82/76}$Se (‰) | 2 s.e.$^{+}$ (‰) | Se (ng·g$^{-1}$) |
|---|---|---|---|---|
| SEC 50-1 | Ret. Eclogite | -1.29 | 0.09 | 86 |
| | | -1.18 | 0.04 | 86 |
| | | -1.19 | 0.06 | 85 |
| | | -1.16 | 0.05 | 84 |
| *(bomb digestion)* | | | | *(83)* |
| (HPA digestion) | | | | *(87)* |
| | *average* | *-1.21* | *0.06* | *85* |
| | *uncertainty (2 s.d.)* | *0.12* | | *1.91* |
| SEC 35-2 | HP serpentinite | 0.11 | 0.08 | 45 |
| | | 0.02 | 0.03 | 46 |
| | average | *0.07* | *0.06* | *46* |
| SEC 36-2 | HP serpentinite | 0.39 | 0.10 | 37 |
| SEC 40-1 | HP serpentinite | 0.35 | 0.08 | 69 |
| | | 0.24 | 0.07 | 67 |
| | *average* | *0.30* | *0.08* | *68* |
| SEC 45-3 | Metapelite | 0.14 | 0.08 | 22 |
| IODP1256D | serpentinized basalt | -0.31 | 0.07 | 170 |
| 309-75R1 | (sheeted dykes) | -0.39 | 0.07 | 169 |
| | *average* | *-0.35* | *0.07* | *170* |
| IODP1256D | Serpentinised basalt | -0.08 | 0.05 | 182 |
| 309-132R1 | (sheeted dykes) | -0.06 | 0.07 | 182 |
| | *average* | *-0.07* | *0.06* | *182* |
| IODP1256D | Gabbro | -0.38 | 0.06 | 201 |

**Table S-4** The $\delta^{82/76}$Se (‰) of the inter-laboratory standard MH−495 (30 ng mL$^{-1}$ Se) measured together with the samples in this study. *Internal precision on a sample run (over 40 cycles) is reported as 2 standard error (2 s.e.).

| | $\delta^{82/76}$Se (‰) | 2 s.e. (‰)* |
|---|---|---|
| | -3.25 | 0.06 |
| | -3.17 | 0.06 |
| | -3.30 | 0.05 |
| | -3.21 | 0.09 |
| | -3.24 | 0.08 |
| | -3.25 | 0.08 |
| | -3.29 | 0.04 |
| | -3.22 | 0.03 |
| | -3.26 | 0.04 |
| | -3.30 | 0.03 |
| | -3.17 | 0.03 |
| | -3.30 | 0.04 |
| | -3.25 | 0.04 |
| | -3.25 | 0.04 |
| | -3.22 | 0.04 |
| | -3.25 | 0.04 |
| | -3.31 | 0.05 |
| | -3.30 | 0.05 |
| | -3.33 | 0.05 |
| *Average* | *-3.26* | |
| *2 s.d.* | *0.09* | |
| | *n = 19* | |

**Table S-5** Se concentrations and isotope compositions of international rock reference material USGS (United States Geological Survey) BCR-2. *Internal precision on a sample run (over 40 cycles) is reported as 2 standard error (2 s.e.).

| Sample | Rock type | $\delta^{82/76}$Se (‰) | 2 s.e.$^{\dagger}$ (‰) | Se (ng·g$^{-1}$) |
|---|---|---|---|---|
| **USGS BCR−2** | basalt | 0.04 | 0.07 | 79 |
| | | 0.22 | 0.06 | 78 |
| | | 0.15 | 0.05 | 78 |
| | | 0.13 | 0.05 | 77 |
| | *average* | *0.14* | | *78* |
| | *2 s.d.* | *0.15* | | *2* |

## *Supplementary Information References*

Evans, K.A., Tomkins, A.G., Cliff, J., Fiorentini, M.L. (2014) Insights into subduction zone sulfur recycling from isotopic analysis of eclogite-hosted sulfides. *Chemical Geology* 365, 1-19.

Halama, R., Bebout, G.E., John, T., Schenk, V. (2010) Nitrogen recycling in subducted oceanic lithosphere: The record in high- and ultrahigh-pressure metabasaltic rocks. *Geochimica et Cosmochimica Acta* 74, 1636-1652.

Halama, R., John, T., Herms, P., Hauff, F., Schenk, V. (2011) A stable (Li, O) and radiogenic (Sr, Nd) isotope perspective on metasomatic processes in a subducting slab. *Chemical Geology* 281, 151-166.

John, T., Scherer, E.E., Schenk, V., Herms, P., Halama, R., Garbe-Schonberg, D. (2010) Subducted seamounts in an eclogite-facies ophiolite sequence: the Andean Raspas Complex, SW Ecuador. *Contribution to Mineralogy and Petrology* 159, 265-284.

Kurzawa, T., König, S., Labidi, J., Yierpan, A., Schoenberg, R. (2017) A method for Se isotope analysis of low ng-level geological samples via double spike and hydride generation MC-ICP-MS. *Chemical Geology* 466, 219-228.

Kurzawa, T., König, S., Alt, J.C., Yierpan, A., Schoenberg, R. (2019) The role of subduction recycling on the selenium isotope signature of the mantle: Constraints from Mariana arc lavas. *Chemical Geology* 513, 239-249.

Labidi, J., König, S., Kurzawa, T., Yierpan, A., Schoenberg, R. (2018) The selenium isotopic variations in chondrites are mass-dependent: Implications for sulfide formation in the early solar system. *Earth and Planetary Science Letters* 481, 212-222.

Li, J.-L., Schwarzenbach, E.M., John, T., Ague, J.J., Huang, F., Gao, J., Klemd, R., Whitehouse, M.J., Wang, X.-S. (2020) Uncovering and quantifying the subduction zone sulfur cycle from the slab perspective. *Nature Communications* 11, 514.

Sadofsky, S.J., Bebout, G.E. (2003) Record of forearc devolatilization in low-T, high-P/T metasedimentary suites: Significance for models of convergent margin chemical cycling. *Geochemistry, Geophysics, Geosystems* 4, 1525-2027.

Shu, Y., Nielsen, S.G., Marschall, H.R., John, T., Blusztajn, J., Auro, M. (2019) Closing the loop: subducted eclogites match thallium isotope compositions of ocean island basalts. *Geochimica et Cosmochimica Acta* 250, 130-148.

Su, W., Schwarzenbach, E., Chen, L., Li, Y., John, T., Gao, J., Chen, F., Hu, X. (2019) Sulfur isotope compositions of pyrite from high-pressure metamorphic rocks and related veins (SW Tianshan, China): Implications for the sulfur cycle in subduction zones. *Lithos* 348-349, 105212.

Varas-Reus, M.I., König, S., Yierpan, A., Lorand, J.-P., Schoenberg, R. (2019) Selenium isotopes as tracers of a late volatile contribution to Earth from the outer Solar System. *Nature Geoscience* 12, 779-782.

Yierpan, A., König, S., Labidi, J., Kurzawa, T., Babechuk, G.B., Schoenberg, R. (2018) Chemical sample processing for combined selenium isotope and selenium-tellurium elemental investigation of the Earth's igneous reservoirs. *Geochemistry, Geophysics, Geosystems* 19, 516-533.

Yierpan, A., König, S., Labidi, J., Schoenberg, R. (2019) Selenium isotope and S-Se-Te elemental systematics along the Pacific-Antarctic ridge: Role of mantle processes. *Geochimica et Cosmochimica Acta* 249, 199-224.